Feasibiliy of optical detection of soft tissue deformation during needle insertion

Christoph Otte[1], Gereon Hüttmann[2] and Alexander Schlaefer[1]

[1] Institute for Robotics and Cognitive Systems, University of Lübeck, Lübeck
[2] Institute for Biomedical Optics, University of Lübeck, Lübeck

Abstract

Needles provide an effective way to reach lesions in soft tissue and are frequently used for diagnosis and treatment. Examples include biopsies, tumor ablation, and brachytherapy. Yet, precise localization of the needle with respect to the target is complicated by motion and deformation of the tissue during insertion.

We have developed a prototypical needle with an embedded optical fiber allowing to obtain optical coherence tomography images of the tissue in front of the needle tip. Using the data and particularly the Doppler information it is possible to estimate the motion of the needle tip with respect to the surrounding soft tissue. We studied whether it is feasible to approximate the depth in tissue by integrating over the relative velocity.

To validate the approach, the needle was driven into tissue phantoms using an articulated robotic arm. The time when the needle entered and left the phantom was observed with optical cameras, and the total motion of the robot was compared with the values computed from the Doppler OCT-measurements.

Our preliminary results indicate that the Doppler data can provide additional information on the needle position inside soft tissue. It could be used in addition to other image data to improve precise needle navigation, particularly when other image modalities are subject to artifacts caused by the needles.

1 Purpose

Precise positioning of needles in soft tissue is a common problem during diagnosis and treatment, e.g., when performing biopsies, tumor ablation or brachytherapy. For instance, up to 14 perineally inserted needles are used for prostate brachytherapy. A so called template with a regular grid of holes is typically used to position and guide the needles during insertion. However, due to the insertion force the tissue is deformed [LMLB05]. This can lead to substantial inaccuracies in the position of the needle with respect to the target region, potentially compromising the treatment [DSPS00, NIT$^+$11, YYN$^+$10].

Generally, image guidance can improve navigation. Yet, the needle itself can cause artifacts in typical image modalities, e.g., phantom echos in ultrasound images. Such artifacts complicate the estimation of the actual depth the needle has traveled through the tissue. For example, while the needle moves the planned distance with respect to the imaging source it may have deformed and compressed tissue in front of the tip, leading to an overestimation of the actual depth in tissue. One approach to consider tissue deformation is to simulate its properties and interaction with the needle [AGPH09]. However, this requires rather detailed modeling of the often unknown tissue parameters.

Medical Imaging 2012: Image-Guided Procedures, Robotic Interventions, and Modeling,
edited by David R. Holmes III, Kenneth H. Wong, Proc. of SPIE Vol. 8316, 83160V
 · doi: 10.1117/12.912538

Another method is to study the forces during needle insertion [MD10]. Again, the actual measurements can depend in a rather complex way on the tissue penetrated by the needle.

In contrast, we propose to obtain information on the relative motion of the needle with respect to the penetrated tissue from within the needle tip. In a previous study we developed a fiber embedded needle for optical coherence tomography (OCT) along the needle path [SOR+10]. The purpose of this study is to investigate whether OCT Doppler data can be used to estimate the amount of tissue that has passed the needle tip during insertion. First, we briefly review the forces and tissue motion during insertion and the basics of Doppler OCT. Second, we describe our experimental setup and the method to compute the depth in tissue. Finally, we present and discuss preliminary results indicating that the motion of the needle tip with respect to soft tissue can be estimated with the proposed approach.

1.1 Doppler OCT

Optical coherence tomography is capable of penetrating up to 3 mm into tissue and produce images with a depth resolution of better than $10\,\mu m$. Based on an interferometer, broadbanded coherent light is used to detect scattering in the probe, e.g., visualizing tissue layers with different refraction indices. Moreover, the phase signal can also be used to study the Doppler effect, i.e., the frequency shift for an observer of an electromagnetic wave moving relative to the source [WMK06]. In the OCT signal the doppler effect causes a phase shift $\Delta\phi$ between adjacent A-scans proportional to the relative velocity ν_{rel} between scatterer and light source, with:

$$\Delta\phi = \frac{4\pi n v_{rel} \Delta t}{\lambda_0} \cdot cos(\theta) \tag{1}$$

Where λ_0 represents the central wavelength of the OCT-System and θ the angle between viewing direction and the scatterers velocity.

The error in the OCT phase signal depends on the signal to noise ratio (SNR)

$$\delta\phi \propto \frac{1}{\sqrt{SNR}} \tag{2}$$

Typically, a smaller SNR leads to an underestimation of the Doppler signal [SSKW08]. Hence, due to the signal decrease caused by scattering and absorption we expect an underestimation of the relative velocity with increasing imaging depth.

1.2 Tissue motion during needle insertion

Force measurements during needle insertion into soft tissue can be used to detect and compensate for deformations. So far, a number of force modeling approaches have been proposed [OSO04, DS03, CSWO05, AKP10]. The insertion force can give an indication of different needle insertion states. Force over depth profiles can be used to distinguish four different conditions [MD10]. During the *loading deformation* the needle does not penetrate, but displace and compress the tissue in axial direction. As a result, the needle force is increasing slowly until the tissue reaches its breaking point. This initiates the *rupture event*. Now tearing of the tissue causes a fast relaxation along the needle axis and the force value drops dramatically. During the *cutting* event, the needle moves smoothly through the tissue and predominantly the friction force between needle and the surrounding tissue is measured. When the needle stops, the tissue starts a slow relaxation, depending on its viscoelastic properties.

The measured needle force is a result of friction, compression and surface tension. These contributions occur in the same direction and are rarely separable [KWC+02]. A further complicating factor

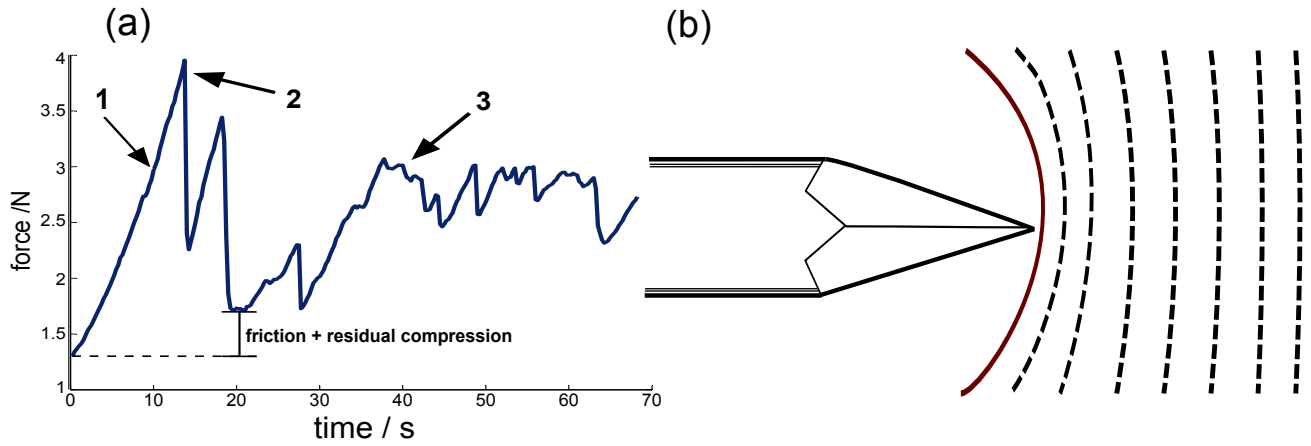

Figure 1: Diagram (a) illustrates the force over time proifle during a needle insertion procedure into a prostate. The force profile shows the loading deformation (1), the tissue rupture (2) and the cutting (3). (b) illustrates the typical deformation during the loading deformation. The tissue layer in front of the needle is pushed in needle direction, until the a rupture occurs.

is the non-elastic character of soft tissue. For example the rupture event (1) in Figure 1 (b) does not cause the entire relaxation of the tissue, but a residual compression along the needle axis remains. Besides that, due to the inhomogenous character of soft tissue the elementary needle inserting states are not always clearly distinguishable. For instance, a multitude of microruptures can occur during the cutting event.

While the same types of tissue motion will be visible when measuring optical data from the needle tip, the measurements are directly related to the actual motion. The OCT Doppler data can be considered as one-dimensional depth profiles of the relative velocity v_{rel} between tissue and needle tip. Hence, the different needle insertion states will be reflected in these profiles. For example, during the preload deformation the tissue compression is expected to occur primarily close to the needle. The relative speed profile should increase from 0 to the needle speed v_{needle} as shown in Figure 2 (a). During the rupture event the relative velocity should show a significant peak and subsequently approach v_{needle} when the needle cuts through the tissue without causing deformation. Note that in the figure the needle is moved by a robot, hence $v_{needle} = v_{rob}$.

Clearly, the amount of tissue deformation caused by a needle depends on the shape of its tip, e.g., as indicated by Podder et al., who observed the needle deflection during insertion in PVC phantoms [PCS+05]. An important consideration for us is the position of the optical fiber. A fiber embedded at the center of a bevel point tip results in an edgeless tip. The reason is the finite diameter of the fiber, which is almost planar at the end. When the fiber is embedded in one side of a trocar point needle, the edge at the tip is preserved. However, the fiber needs to be covered by epoxy resin leading to a slight change in the refraction index. Moreover, this adds an offset between needle tip and OCT fiber. Eventually we have studied two different needles, one with bevel point and one with trocar tip. In either case the needle tip results in a combination of axial and lateral tissue motion and compression around the needle tip. We therefore consider a correction factor k which is determined in an initial calibration step and adjusts for the portion of the tissue motion measured in axial direction. Note that k depends on the measurement depth and the tip shape.

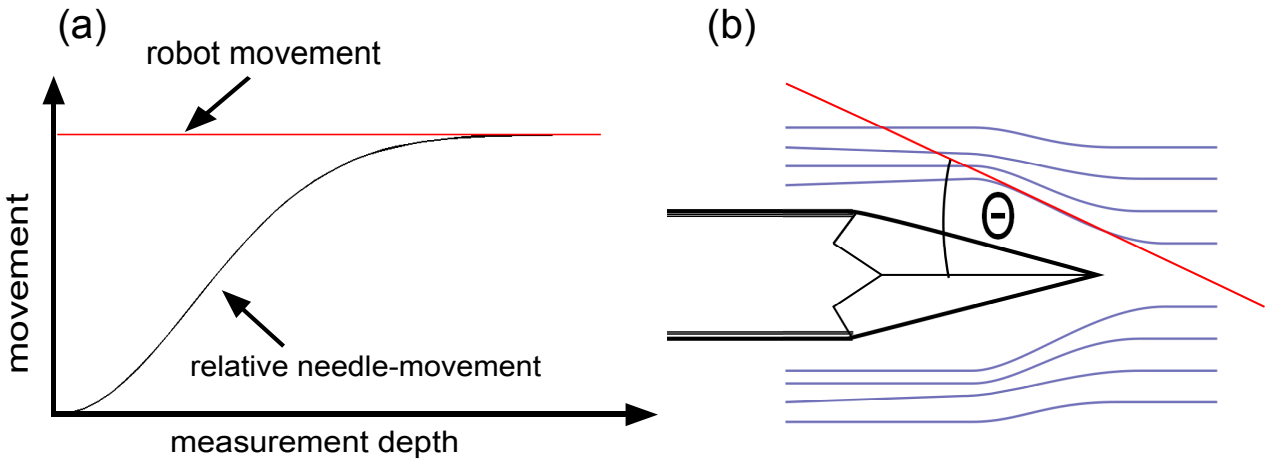

Figure 2: Diagram (a) shows a distribution of relative velocity between a robot driven needle and tissue over the axial distance to the needle tip. The needle does not penetrate but push the tissue, deformations along the needle axis occur. Assuming homogenous mechanical properties in the tissue, one would expect the integral deformation to appear directly in front of the needle. Related to this, the relative velocity between needle and tissue starts with nearly zero and increases with further depth until it is equal to the robot driven speed. Figure (b) illustrates how the tissue flows around the needle tip during the cutting phase. Relative movement between needle and tissue occurs with the angle θ.

2 Methods

2.1 Hardware Setup

The hardware setup is shown in Figure 4. We use a modified needle with an embedded optical fiber, which is connected to an OCT-System (Callisto, Thorlabs) with a central wavelength of 930 nm, a depth resolution of up to 7 µm and 1200 Hz A-scan rate. The needle is driven by an industrial robot (Adept Viper s850) with a positioning accuracy of 30 µm. A camera Logitech Pro 9000 with a resolution of 1280 x 720 pixels and a frame rate of 30 fps is used to monitor the exit of the needle. All modalities are connected to a single computer which collects the data synchronously. Furthermore, LabView, MatLab, and vcapg2-plugin [Kob01] are used to control the OCT-system and the robot, and to process the camera data. The tissue sample is fixed in a holder placed in front of the camera, and the latter is used to detect when the needle leaves the - possibly deformed - tissue.

In our experiments, we use two different custom made needles based on 18 gauge brachytherapy needles. We replaced the original needle tips with modified aluminium trocar and bevel point tips. In both needles we embedded an optical fiber Thorlabs 780HP with a convex self focusing tip geometry. The fiber is embedded in the central tip on the bevel point design and peripheral on a surfaces in the trocar point geometry, see Figure 4 (b). To preserve the fiber tip from physical damage, the boreholes are filled with epoxy resin. We denote the distance between the end of the fiber and the needle point by z_0, which is $z_{0bevel} = 0\ mm$ and $z_{0trocar} = 0.83\ mm$ for the bevel point and trocar tip, respectively.

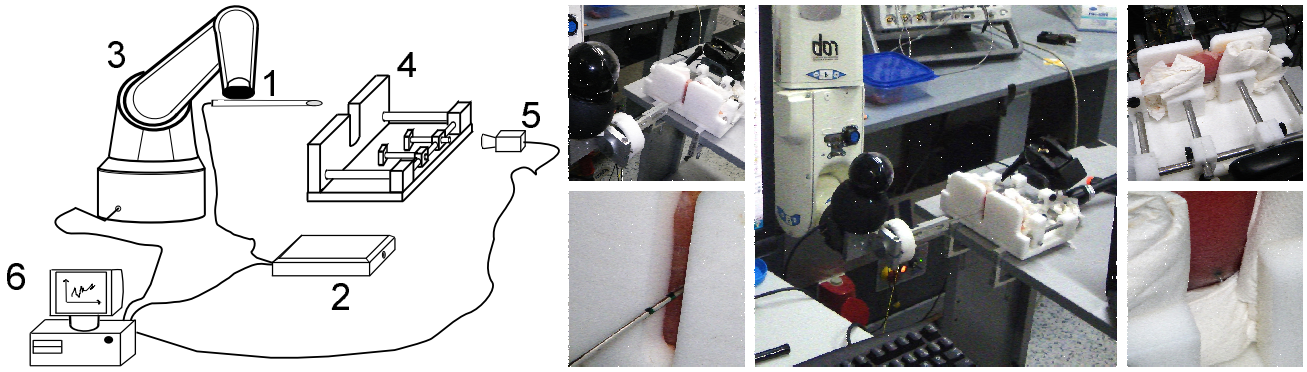

Figure 3: (a) Experimental setup: The needle (1) includes an optical fiber and is connected to an OCT-System (2). An industrial Robot (3) drives the needle trough the sample holder (4), while a camera (5) is there to detect outcome events. All modalities are connected to a single computer (6). On the right the actual components and the needle entry and exit are shown.

2.2 Entry, exit and velocity estimation

The needle entry into the tissue is detected in the OCT signal. When the needle touches the tissue the signal in the distance z_0 (Figure 4) increases over a certain threshold. Our camera in front of the probeholder is used to detect the exit event with a simple threshold on the red channel. As soon as the needle leave the tissue the OCT light leads to a distinctive red spot.

To calculate the velocity profile $v(z)$ we take the phase angles of the complex OCT signal $\tilde{S} = S_0(t,z)e^{(i\phi(t,z))}$ and calculate the difference between adjacent A-scans. The value range of the phase signal is limited to $\phi \in \mathbb{R}$. Setting this in equation 1 leads to equation 3.

$$\|v\| \leq \frac{f_a \lambda}{4n} \tag{3}$$

This results in a maximum measurable velocity of $0.2mm/s$. Assuming that equation 3 holds [AKA+09] we obtain the distance traveled in the tissue by summing the velocities multiplied by the sampling interval $T = \frac{1}{f_a}$.

2.3 Needle calibration

To compensate for the needle geometry we calculate the correction factor k for the bevel and trocar point tips using gelatin phantoms. Due to the homogenous structure of the phantoms we expect little tissue deformation, which is often related to boundary layers in real tissue. Calibration works as follows: First, the robot drives the needle slowly towards the surface until the tissue is detected in the OCT signal. Second, the robot drives and additional distance of $d_{rob} = 10mm$ into the tissue. This is done in M steps of d_{rob} each. Finally, the distance computed from the OCT signal denoted by d_{meas} is compared to the actual robot motion.

The calibration was repeated N times and finally the median of all absolute differences between d_{rob} and d_{meas} was determined and the factor k computed accordingly. We used $N = 5$, $M = 20$, and $d_{rob} = 0.5\ mm$ to calibrate the two needles. To account for measurement depth and noise we compute the maximum velocity and hence d_{meas} in a depth window in front of the needle.

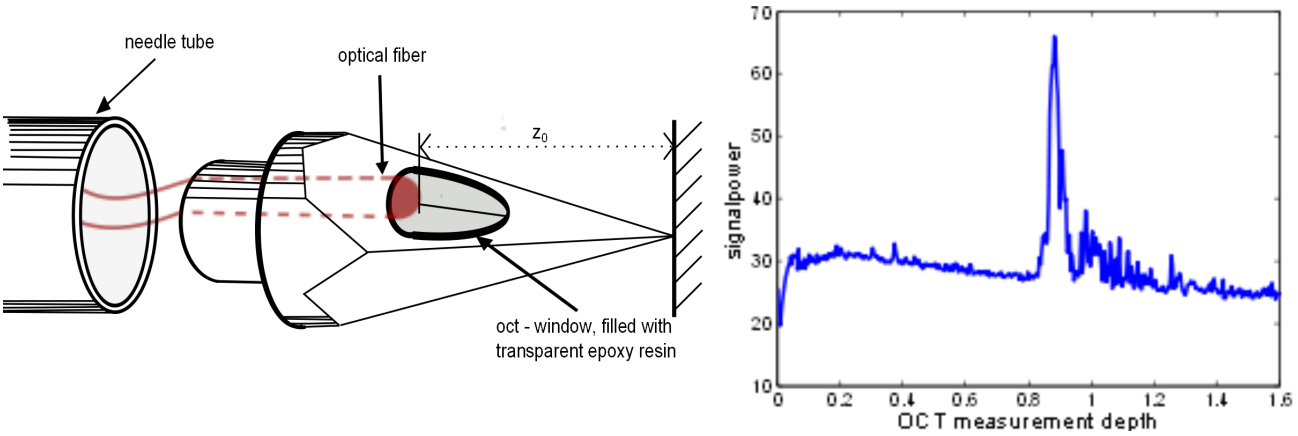

Figure 4: Modified brachytherapy needle: The optical fiber is embedded in an aluminium trocar point tip. The borehole is filled up with transparent epoxy resin to preserve the geometry. The whole tip is then glued into the stump of an cutted brachytherapy needle. The diagram shows the oct signal when the needle tip touches a flat surface. The distance z_0, where the signal is increasing is related to distance between fiber and needle tip, i.e., approximately 0.8 mm in the figure.

2.4 Data acquisition

Our experimental validation is based on synthetic and tissue phantoms. To get a reproducable phantom with well defined optical and mechanical properties we used gelatin with added TiO_2 powder. The TiO_2 results in good scattering and hence suitable OCT signals, and the gelatin can be penetrated by the needle with little friction and deformation. For the experiments the gelatin was placed in a small plastic cup.

The actual tissue tests where done in pork belly using the bevel point needle. To estimate the initial thickness of the tissue it was placed between two parallel metal plates and the distance between the plates was measured. Subsequently, the tissue was placed in the holder and the needle completely moved through the sample. Note that the clamps holding the tissue where spaced at approximately $15mm$. This was necessary to reduce the risk of running the needle into the plastic if the former got deflected during insertion.

3 Results

Results for needle calibration are shown in Figure 5. The histograms show a distribution of the measured distance per robostep the needle moved relative to the tissue. A tight histogram implies a good reproducibility, while a stretched histogram implies a huge mean variation. The data comes from 5 single measurements with 20 steps. The bevel point geometry clearly shows a peak between 0.3 mm and 0.35 mm. The difference between step size and measured distance is nearly constant. The calculated calibration factor is $k = 3.05mm$. In contrast the trocar point needle shows a widely dispersed histogram. The calibration factor here is $k = 3.36$.

Figure 6 gives results for four needle insertions of the bevel tip needle into an approximately 15 mm thick piece of pork belly. The actual robot motion from entry to exit ranges from 80 to 98 steps or 40 mm to 49 mm, indicating substantial deformation of the tissue. However, all four traces show agreeing depth of approximately 12 mm when using the original correction factor k obtained from

calibration.

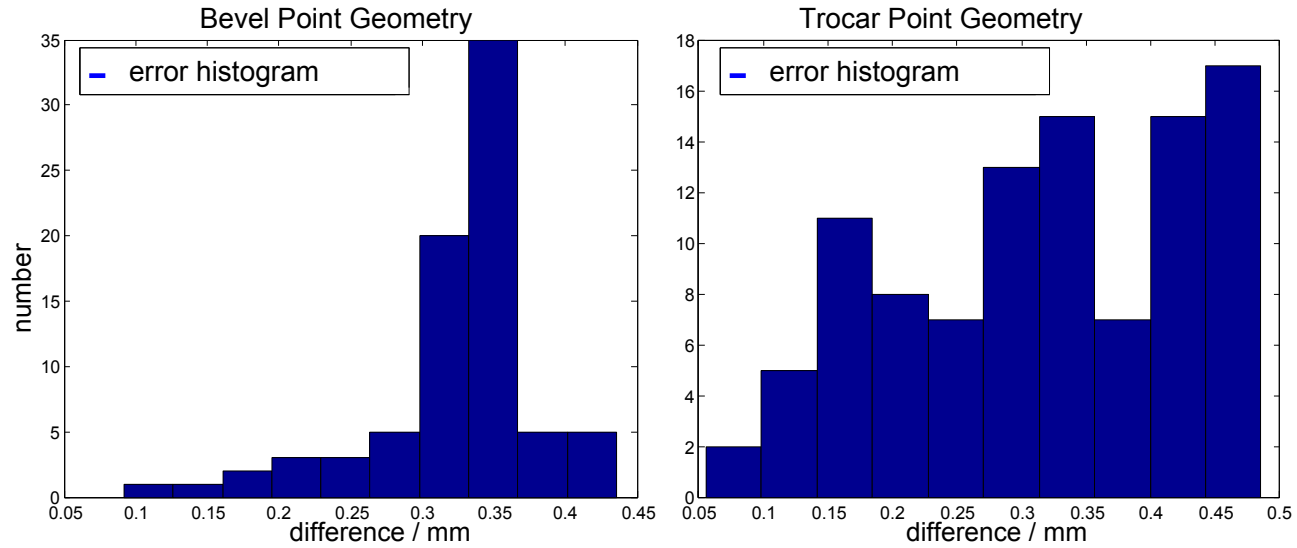

(a) error histogram with the differences between driven and measured stepsize in gelantine phantoms

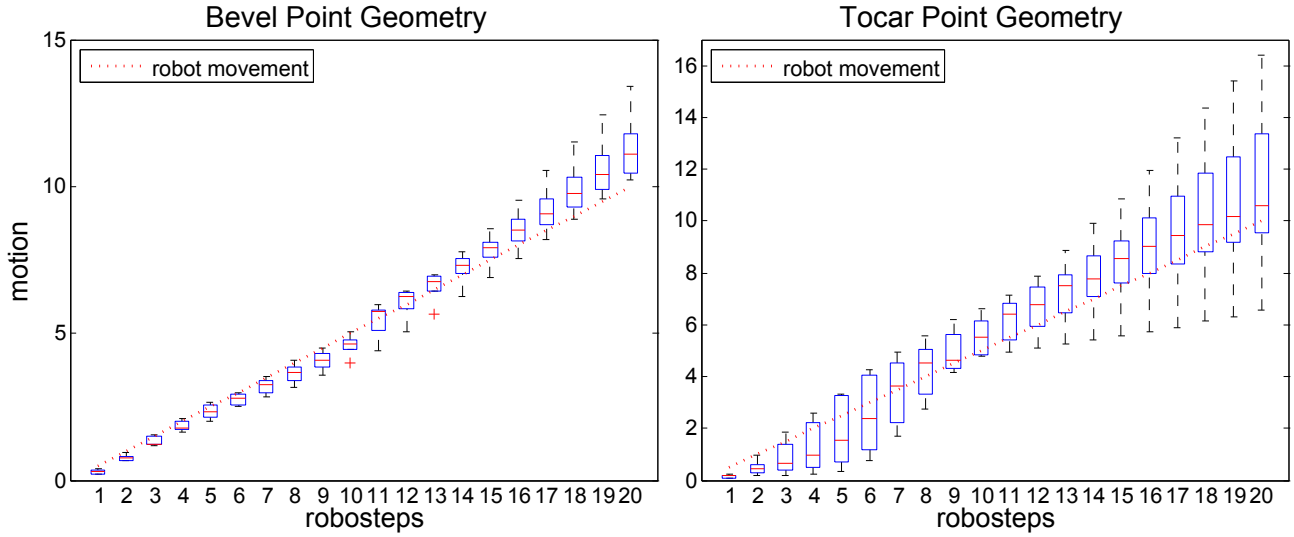

(b) boxplot with the cumulated relative movement and the robot driven movement in gelantine phantoms

Figure 5: (a) shows a distribution of the differences between step size of the robot and the measured distance between needle and tissue. A significant peak, like in the bevel point diagram, indicates, the the difference between driven and measured distance is constant over the robot steps, while a widely distributed histogram, like the trocar point histogram, indicates large deviations. Figure(b) shows a boxplot with the cumulated sum of the single steps from 5 times repeated measurements compared to the robot driven movement. The estimated movement is multiplied by the correction factor k with $k_{bevel} = 3.05$ and $k_{trocar} = 3.36$. The measurement with the bevel point tip show less deviations compared to the trocar point tip.

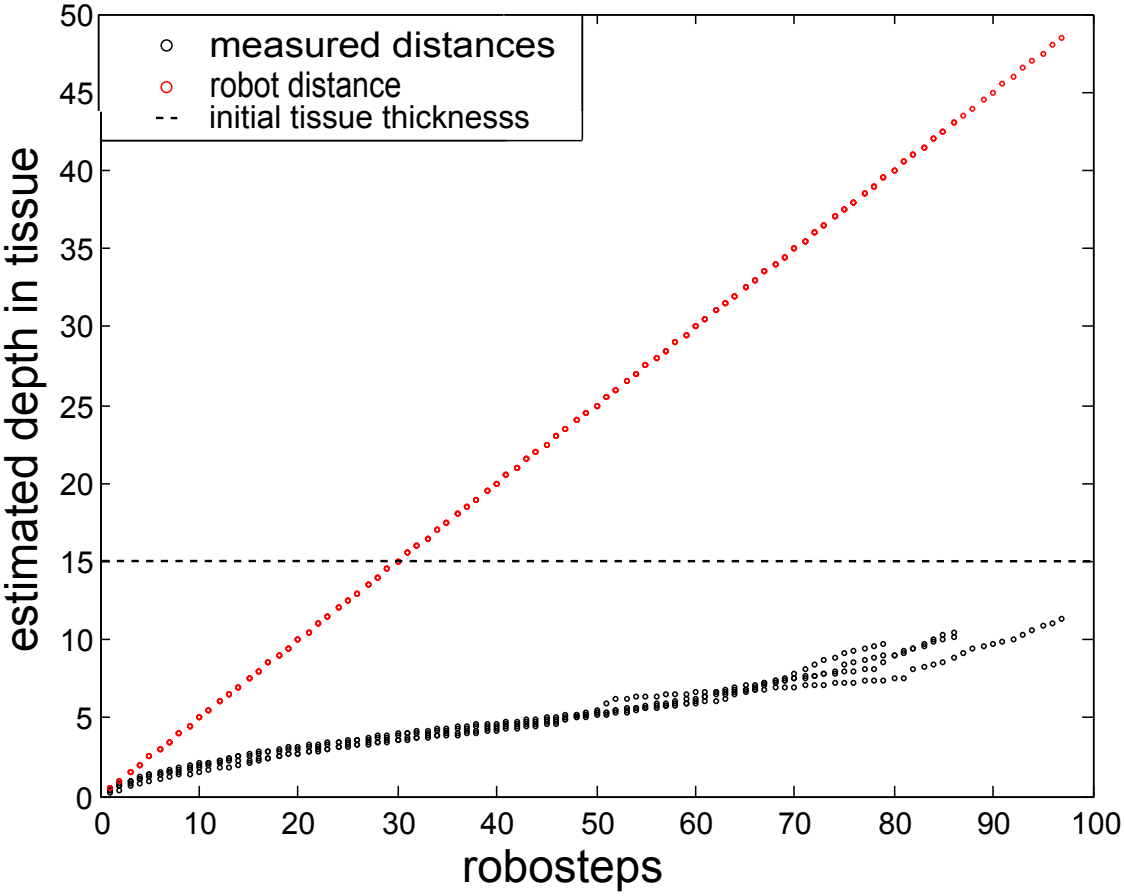

Figure 6: The Diagram shows the four times repeated measurement in pork belly with the bevel point tip, multiplied by the factor k_{bevel}. While the initial thickness of the meat was measured with d_{init} 15 mm, the robot drives the needle for about 50 mm until the camera detects the outcome event. In contrast the measured relative needle tissue distance is close to, but smaller than the initial tissue thickness.

4 Discussion

We presented an experimental setup and results illustrating that Doppler OCT measurements can be used to estimate the relative motion between a needle and soft tissue. Using the bevel point needle it was possible to obtain reproducible velocity and motion values in a gelatin phantom and in pork belly.

In pork belly the robot has to drive the needle up to five times further than the initial tissue thickness. This is expected, as the tissue is deforming along the needle path, i.e., the robot motion

trial No.	tissue thickness	driven distance	rel. error / %	estimated distance	rel. error / %
1	15	48.5	223.33	11.45	23.67
2	15	43.0	186.67	13.35	11.0
3	15	43.0	186.67	13.39	10.72
4	15	39.5	163.33	11.45	23.67
mean	15	43.5	190.00	12.41	17.26

Table 1: Comparison between initial tissue thickness, driven distance and estimated distance. The overall driven distance is up to 3 times higher ($48.5mm$), than the initial tissue thickness, while the corresponding doppler measurement shows a relative movement between needle and tissue about $11.45mm$. The average error is 190% between initial thickness and driven distance and 21% between initial thickness and estimated distance. All distances are given in mm.

does not lead to an equal motion through the tissue. The estimated motion traveled through the whole pork belly is smaller than the initial tissue thickness.

On the one hand, this could be attributed to a compression of the tissue, i.e., the needle passes compressed, more dense, tissue. Potentially, the actual tissue compression could be taken into a count by an additional compression factor. Moreover, fast movements caused by small tissue ruptures do potentially not fulfill equation 3 and the OCT misses the movement.

On the other hand a tissue specific calibration may resolve the remaining error, as the correction factor established for the gelatin phantom lead to a substantial but constant underestimation of the actual motion. It would be interesting to study whether this is related to the gelatin phantom itself, e.g, due to small inhomogenities like minor air bubbles causing unexpected deformations. While camera based optical tracking has been proposed [CSWO05], this procedure is incompatible with the scattering agent added to our phantom.

Interestingly, although it is pointier, our design of a trocar shaped needle tip did not lead to reproducible velocity estimation from OCT Doppler data. Explanations could be the asymmetric shape and the off-center location of the optical fiber. Considering the results from Podder et al. the lower transverse insertion force for bevel point needles compared to trocar point needles may also have an impact [PCS$^+$05].

All in all the results indicate that there is a correlation between Doppler OCT based motion estimation and actual motion in tissue. This information could be used on its own, or potentially be combined with force measurements. It has been shown that rapid tissue relaxations which may be undetectable for our OCT system are strongly related to a drop in the insertion force [OAK$^+$11, MD10]. However, force measurement on the needle base can provide information about events on the needle tip, due to rapid changes in the force value. Certainly, the absolute value is influenced by different side effects, e.g., friction force between needle and tissue. A force measurement on directly on the needle tip would be desirable, but actual approaches allow uniaxial force measurement only [KWC$^+$02]. Hence, it would be interesting to study whether a combination of force measurements on the needle base [OSO04, CSWO05, AKP10] can be combined with the OCT motion estimation to further improve needle navigation in soft tissue.

5 Conclusion

We presented a novel approach to estimate the motion of a needle with respect to soft tissue based on Doppler OCT from within the needle tip. Our results indicate that the measured data is correlated to

the actual motion. A tissue dependent calibration is required and artifacts due to very fast motion or extreme compression need to be considered. Advantages include the absence of needle artifacts and a high sampling rate, which would allow for real-time control, e.g., of a robotic needle driver.

References

[AKA+09] S. G. Adie, B. F. Kennedy, J. J. Armstrong, S. A. Alexandrov, and D. D. Sampson. Audio frequency in vivo optical coherence elastography. *Phys. Med. Biol*, 54(10):31293139, 2009.

[AGPH09] Ron Alterovitz, Kenneth Y Goldberg, Jean Pouliot, and I-Chow Joe Hsu. Sensorless motion planning for medical needle insertion in deformable tissues. *IEEE Trans Inf Technol Biomed*, 13(2):217–225, Mar 2009.

[AKP10] A. Asadian, M. R. Kermani, and R. V. Patel. A compact dynamic force model for needle-tissue interaction. *EMBC 2010*, 2010:2292–2295, 2010.

[CSWO05] Jessica R Crouch, Chad M Schneider, Josh Wainer, and Allison M Okamura. A velocity-dependent model for needle insertion in soft tissue. *MICCAI 2005*, 8:624–32, 2005.

[DSPS00] Steven J Damore, A.M.Nisar Syed, Ajmel A Puthawala, and Anil Sharma. Needle displacement during hdr brachytherapy in the treatment of prostate cancer. *International Journal of Radiation Oncology*, 46(5):1205–1211, 2000.

[DS03] Simon P DiMaio and S E Salcudean. Needle insertion modeling and simulation. *IEEE TRANSACTIONS ON ROBOTICS AND AUTOMATION*, 19(5):864–75, 2003.

[KWC+02] H. Kataoka, T. Washio, K. Chinzei, K. Mizuhara, C. Simone, and A. Okamura. Measurement of the tip and friction force acting on a needle during penetration. *MICCAI*, 2488:216–223, 2002.

[Kob01] Kazuyuki Kobayashi. *MATLAB Utilization Book*. Shuwa System Co, Ltd., 2001.

[LMLB05] V Lagerburg, M A Moerland, J J Lagendijk, and J J Battermann. Measurement of prostate rotation during insertion of needles for brachytherapy. *Radiotherapy and Oncology*, 77(3):318–23, 2005.

[MD10] Mohsen Mahvash and Pierre E. Dupont. Mechanics of dynamic needle insertion into a biological material. *IEEE TRANSACTIONS ON BIOMEDICAL ENGINEERING*, 57(4):934 – 943, 2010.

[NIT+11] R. Nakamura, H. Ishiyama, S. Tanji, T. Satoh, H. Oikawa, W Inatsu, S Ehara, and Hayakawa K. Effects of ellipsoid prostate deformation on dose delivery during permanent interstitial brachytherapie. *Brachytherapy*, 10(3):208–213, 2011.

[OSO04] Allison M Okamura, Christina Simone, and Mark D OLeary. Force modeling for needle insertion into soft tissue. *IEEE TRANSACTIONS ON BIOMEDICAL ENGINEERING*, 51(10):1707–1716, 2004.

[OAK+11] C. Otte, R. Ansari, G. Kovcs, M. Sommerauer, G. Hüttmann, and A. Schlaefer. Kompensation von bewegungsartefakten beim einbringen von brachytherapienadeln. *BVM 2011*, 2011:444–448, 2011.

[PCS+05] T K Podder, D P Clark, J Sherman, D Fuller, E M Messing, D J Rubens, J G Strang, Y D Zhang, W ODell, W S Ng, and Y Yu. Effects of tip geometry of surgical needles: An assessment of force and deflection. *IFMBE 2005*, 2005:1641–1644, 2005.

[SOR+10] A. Schlaefer, C. Otte, L. Richter, M. Heinig, R. Bruder, G. Kovacz, and G. Hüttman. Towards high resolution image guided needle navigation in prostate brachytherapie. *CARS 2010*, 2010:24–25, 2010.

[SSKW08] A Szkulmowska, M Szkulmowski, A Kowalczyk, and M Wojtkowski. Phase-resolved doppler optical coherence tomography-limitations and improvements. *Opt Let*, 33(13):1425–1427, 2008.

[WMK06] R. K. Wang, Z. H. Ma, and S. J. Kirkpatrick. Tissue doppler optical coherence elastography for real time strain rate and strain mapping of soft tissue. *Appl. Phys. Lett*, 89(14):144103–3, 2006.

[YYN+10] K. Yoshida, H. Yamazaki, T. Nose, H. Shiomi, M. Yoshida, M. Mikami, T. Takenaka, T. Kotsuma, E.Tanaka, K. Kuriyama, Y. Harada, A. Tohda, Y. Yasunaga, and T. Oka. Needle applicator displacement during high-dose-rate interstitial brachytherapy for prostate cancer. *Brachytherapy*, 9(1):36–41, 2010.